

Manuscript Number: NIMA-D-19-00297R2

Title: Commissioning of the ACTive TARget and Time Projection Chamber
(ACTAR TPC)

Article Type: Full length article

Section/Category: High Energy and Nuclear Physics Detectors

Keywords: Active target; Time projection chamber; Micromegas; Resonant
scattering

Corresponding Author: Dr. Benoit Mauss,

Corresponding Author's Institution:

First Author: Benoit Mauss

Order of Authors: Benoit Mauss; Pierre Morfouace; Thomas Roger; Julien
Pancin; Gwen Grinyer; Jérôme Giovinazzo; Valérien Alcindor; Hector
Alvarez-Pol; Alex Arokiaraj; Mathieu Babo; Beyhan Bastin; Catalin Borcea;
Manuel Caamano; Simone Ceruti; Beatriz Fernandez-Dominguez; Emilie
Foulon-Moret; Patrice Gangnant; Simon Giraud; Alex Laffoley; Giorgia
Mantovani; Tommaso Marchi; Belén Monteagudo; Jérôme Pibernat; Oleksii
Poleshchuk; Riccardo Raabe; Jonas Refsgaard; Aldric Revel; Frederic
Saillant; Mihai Stanoiu; Gilles Wittwer; Jie Cheng Yang

Abstract: The ACTive TARget and Time Projection Chamber (ACTAR TPC) is a
novel gas-filled detector that has recently been constructed at GANIL.
This versatile detector is a gaseous thick target that allows the
tracking of charged particles in three dimensions and provides a precise
reaction energy reconstruction from the vertex position. A commissioning
experiment using resonant scattering of a 3.2 MeV/nucleon ^{180}Ar beam on an
isobutane gas (proton) target was performed. The beam and the heavy
scattered ions were stopped in the gas volume, while the light recoil
left the active volume and were stopped in auxiliary silicon detectors. A
dedicated tracking algorithm was applied to determine the angle of
emission and the length of the trajectory of the ions, to reconstruct the
reaction kinematics used to build the excitation functions of the
 $^{1}\text{H}(^{180,180}\text{Ar})^{1}\text{H}$ and $^{1}\text{H}(^{180,15}\text{N})^4\text{He}$ reactions. In this article, we describe
the design of the detector and the data analysis, that resulted in center
of mass reaction energy resolutions of 38(4) keV FWHM and 54(9) keV FWHM
for the proton and alpha channels, respectively.

Commissioning of the ACTive TARget and Time Projection Chamber (ACTAR TPC)

B. Mauss^{a,1,*}, P. Morfouace^a, T. Roger^{a,*}, J. Pancin^a, G.F. Grinyer^{a,b}, J. Giovinazzo^c, V. Alcindor^a, H. Álvarez-Pol^d, A. Arokiaraj^e, M. Babo^f, B. Bastin^a, C. Borcea^g, M. Caamaño^d, S. Ceruti^e, B. Fernández-Domínguez^d, E. Foulon-Moret^a, P. Gangnant^a, S. Giraud^a, A. Laffoley^h, G. Mantovaniⁱ, T. Marchiⁱ, B. Monteagudo^j, J. Pibernat^c, O. Poleshchuk^e, R. Raabe^e, J. Refsgaard^e, A. Revel^{a,j}, F. Saillant^a, M. Stanoiu^g, G. Wittwer^a, J. Yang^e

^aGrand Accélérateur National d'Ions Lourds (GANIL), CEA/DRF-CNRS/IN2P3, Bvd Henri Becquerel, 14076 Caen, France

^bDepartment of Physics, University of Regina, Regina, SK S4S 0A2, Canada

^cCentre d'Études Nucléaires de Bordeaux Gradignan (CENBG) - UMR 5797, CNRS/IN2P3 - Université de Bordeaux, Chemin du Solarium, F-33175 Gradignan, France

^dDpt. de Física de Partículas Univ. of Santiago de Compostela and IGFAE, E-15758, Santiago de Compostela, Spain

^eKU Leuven, Instituut voor Kern- en Stralingsfysica, 3001 Leuven, Belgium

^fInstitut de Physique Nucléaire, CNRS/IN2P3, Université Paris-Sud, Université Paris-Saclay, F-91406 Orsay, France

^gIFIN HH, str. Reactorului 30, P. O. Box MG 6, Bucharest-Magurele, Romania

^hDepartment of Physics, University of Guelph, Guelph, ON N1G 2W1, Canada

ⁱINFN Laboratori Nazionali di Legnaro, 35020 Legnaro, Italy

^jLPC Caen, Normandie Université, ENSICAEN, Université de Caen, CNRS/IN2P3, F-14050, Caen, France

Abstract

The ACTive TARget and Time Projection Chamber (ACTAR TPC) is a novel gas-filled detector that has recently been constructed at GANIL. This versatile detector is a gaseous thick target that allows the tracking of charged particles in three dimensions and provides a precise reaction energy reconstruction from the vertex position. A commissioning experiment using resonant scattering of a 3.2 MeV/nucleon ^{18}O beam on an isobutane gas (proton) target was performed. The beam and the heavy scattered ions were stopped in the gas volume, while the light recoil left the active volume and were stopped in auxiliary silicon detectors. A dedicated tracking algorithm was applied to determine the angle of emission and the length of the trajectory of the ions, to reconstruct the reaction kinematics used to built the excitation functions of the $^1\text{H}(^{18}\text{O}, ^{18}\text{O})^1\text{H}$ and $^1\text{H}(^{18}\text{O}, ^{15}\text{N})^4\text{He}$ reactions. In this article, we describe the design of the

37 detector and the data analysis, that resulted in center of mass reaction energy
38 resolutions of 38(4) keV FWHM and 54(9) keV FWHM for the proton and alpha
39 channels, respectively.
40 *Keywords:* Active target, Time projection chamber, MICROMEGAS, Resonant
41 scattering

42 1. Introduction

43 The study of nuclear matter far from the valley of stability has led to signif-
44 icant changes in terms of techniques used to study exotic nuclei when compared
45 to studies of stable nuclei. The dramatic decrease in intensity for radioactive
46 ion beams, and the inherent need to work in inverse kinematics (the beam is the
47 heavy particle, as no target can be made with short lived radioactive nuclei),
48 has to be compensated with the use of thicker targets. This, unfortunately,
49 decreases the overall resolution that can be obtained on the determination of
50 the final state parameters, such as the excitation energy. To cope with these
51 challenges, active targets were developed a few decades ago as summarized in
52 a recent review article [1]. These detectors are usually based on the concept
53 of Time Projection Chambers (TPC). Using the detection medium as a target
54 for nuclear reactions, they are used to track charged particles, extract reaction
55 vertices and thus correct the energy lost by charged particles inside the target.
56 The first active target built for nuclear physics experiments was the IKAR setup
57 at GSI [2], which was constructed to study exotic light-ion matter distributions.
58 Since then, more versatile instruments were developed such as the active target
59 MAYA at GANIL [3] that was used to study transfer reactions on light exotic
60 nuclei [4–6] and giant resonances in Ni isotopes [7, 8]. At about the same time,
61 the CENBG TPC [9] was developed to investigate exotic radioactivity modes,
62 such as two proton radioactivity [10]. With the advent of new digital electron-
63 ics developments, such as the General Electronics for TPCs project (GET) [11],
64 next generation active targets and time projection chambers with more precise
65 volume sampling have been constructed or are planned worldwide [1, 12–15].

66 The ACTIVE TARget and Time Projection Chamber (ACTAR TPC) is a
 67 state-of-the-art detector developed by a collaboration of European laboratories
 68 and built at GANIL. It has a charge projection plane segmented in 128×128
 69 square pads of $2 \times 2 \text{ mm}^2$ connected to the GET system. With GET, the sig-
 70 nal can be digitized at several user-specified frequencies in 512 time cells per
 71 channel, sampling the active volume in 8 Mega voxels. This article presents the
 72 performances of ACTAR TPC using the $^1\text{H}(^{18}\text{O}, ^{18}\text{O})^1\text{H}$ and $^1\text{H}(^{18}\text{O}, ^{15}\text{N})^4\text{He}$
 73 resonant reactions performed during a 20-hour commissioning experiment at
 74 GANIL.

75 **2. Experimental set-up**

76 *2.1. Detector description*

77 The ACTAR TPC detector, shown schematically in Figure 1, follows the
 78 construction of two 8-times smaller demonstrator [16, 17] using different tech-
 79 nologies for the pad wiring. The internal skeleton of ACTAR TPC chamber
 80 measures $606 \text{ mm} \times 606 \text{ mm} \times 335 \text{ mm}$. The gas input and output are positioned
 81 on opposite corners of the chamber to ensure a good overall homogeneity of the
 82 gas or gas mixtures. All flanges around the structure are made with 1.5 cm thick
 83 aluminum in order to sustain up to one bar differential pressure with minimum
 84 deformation. In order to put the $6 \mu\text{m}$ thick Mylar beam-entrance window as
 85 close as possible to the wire field cage, the front flange is equipped with a cylin-
 86 drical nose with a diameter of 80 mm. This design reduces the distance from the
 87 entrance window to the active volume of the detector to only 60 mm, as shown
 88 in Figure 1. The bottom and top flanges are used to mechanically support the
 89 drift cage and provide the necessary connections to the pixelated anode, respec-
 90 tively. The side flanges can be used to hold auxiliary detectors, depending on
 91 the needs of the particular physics experiments.

92 The active volume is surrounded by a $295 \text{ mm} \times 295 \text{ mm} \times 255 \text{ mm}$ double-
 93 wire field cage that is attached to the cathode and is fed via a 20 kV high voltage
 94 feedthrough on the bottom flange. The field cage consists of $20 \mu\text{m}$ diameter

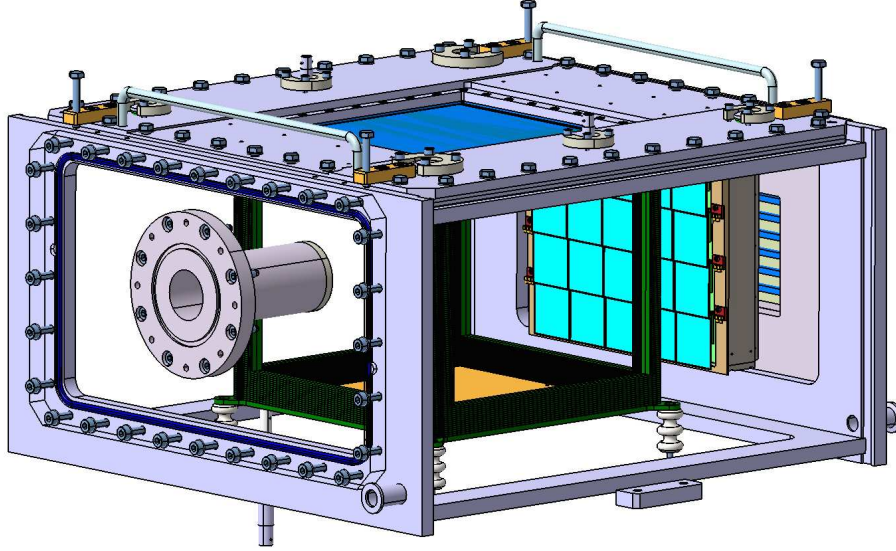


Figure 1: 3D computer-aided drafting (CAD) drawing of ACTAR TPC. See text for details.

95 wires with a 1 mm pitch on the inner plane and a 2 mm pitch on the outer
 96 plane, connected through $4.7\text{ M}\Omega$ resistors. As explained in Ref. [16], the use
 97 of two field degradation planes ensures a good homogeneity of the drift field by
 98 preventing the electric field between the drift cage and the auxiliary detectors
 99 to leak into the drift region.

100 With the drift electric field, ionization electrons produced in the active re-
 101 gion drift towards the anode that is highly segmented into 128×128 square
 102 pads, each with a side edge of 2 mm. The resulting high density of channels
 103 (25 channels/cm^2 , 16384 total pads) was therefore a challenge for designing the
 104 mechanics and pad connections while ensuring minimal mechanical deformation
 105 of the flange when applying up to 1 bar differential pressure. Typical exper-
 106 iments are performed with pressures ranging from a few tens of mbar up to
 107 one bar. Our solution was to build the anode from a metal-core printed circuit
 108 board (PCB) with a direct connection through the circuit from the pads to a
 109 connector with a 2 mm pitch (size of a pad), as described in Ref. [17].

110 Based on the demonstrator detector design [16], the pad plane for ACTAR

111 TPC was equipped with a $\simeq 220\,\mu\text{m}$ gap bulked MICROMEGAS amplification
 112 system [18, 19] made by the CERN PCB Workshop. Usually, the amplification
 113 gap in MICROMEGAS is about $100\,\mu\text{m}$, which is the optimum gap for atmospheric
 114 pressure operation. Here, the large amplification gap was chosen based on the
 115 study in Ref. [20] where good amplification was achieved even at low pressures
 116 (below 300 mbar).

117 The 16384 pads are connected through flex Kapton spark-protection circuits
 118 (ZAP) to the 64 ASIC and ADC (AsAd) boards of the GET system. The AsAd
 119 are arranged perpendicular to the beam axis in order to minimize the amount
 120 of channels per AsAd board hit by the beam, hence reducing the dead time
 121 as explained in Ref. [11]. The AsAd boards are connected to 8+8 Concentra-
 122 tion Boards (CoBo) cards held in two Micro Telecommunications Computing
 123 Architecture (μTCA) crates. Two Multiplicity, Trigger and Time (MuTanT)
 124 modules (one master and one slave) are used to distribute the 100 MHz clock
 125 to the CoBo boards, and distribute the trigger to GET. The μTCA crates car-
 126 rier hubs (MCH) are connected through their 10 Gb interface to a PowerEdge
 127 R730xd Dell acquisition server equipped with two Intel Xeon E5-2630 v4 central
 128 processing units (CPU).

129 For the present study, as seen in Figure 1, the downstream flange of ACTAR
 130 TPC was covered with twenty $5 \times 5\,\text{cm}^2$ and $700\,\mu\text{m}$ thick silicon detectors (Si)
 131 that were used to detect the scattered protons escaping the active volume. They
 132 were each equipped with 10 mV/MeV charge-sensitive preamplifiers that fed
 133 CAEN N568 amplifiers with $3\,\mu\text{s}$ shaping time and $\times 32$ gain. The shaped output
 134 of the module was connected to GANIL VXi peak-sensing ADCs. The fast
 135 output of the amplifiers was discriminated in CAEN N844 modules and used to
 136 trigger the GAMER VXi trigger module. The VXi electronics coupling to the
 137 GET system was made using the CENTRUM protocol [21] with the GAMER
 138 VXi used as master trigger for the whole electronics setup.

139 *2.2. Settings of the commissioning*

140 The ACTAR TPC commissioning experiment was performed at GANIL.
141 The goal was to estimate the capabilities of the detector for performing reso-
142 nant scattering studies. A low-energy ^{18}O beam was chosen to benchmark the
143 resolution of the detector based on the reconstruction of the excitation function
144 of the $^1\text{H}(^{18}\text{O}, ^{18}\text{O})^1\text{H}$ and $^1\text{H}(^{18}\text{O}, ^{15}\text{N})^4\text{He}$ reactions.

145 An ^{18}O beam was accelerated to 6.6 MeV/nucleon in the CSS1 cyclotron
146 and was sent to the G3 experimental hall where ACTAR TPC was mounted
147 on the beam line. The beam was slowed down using a $63\,\mu\text{m}$ thick aluminum
148 degrader and reached the beginning of the active volume with an energy of
149 3.2 MeV/nucleon. This lower energy allowed states in ^{19}F to be populated be-
150 tween 8 and 11 MeV in excitation energy. The incoming intensity was monitored
151 using a collimated multiwire proportional counter (MWPC) that was placed in
152 front of the entrance window of ACTAR TPC. During the 20 hours of data
153 taking, the average ^{18}O beam intensity was 1.5×10^4 particles per second. The
154 proton target used to study the $^1\text{H}(^{18}\text{O}, ^{18}\text{O})^1\text{H}$ and $^1\text{H}(^{18}\text{O}, ^{15}\text{N})^4\text{He}$ reactions
155 was isobutane (iC_4H_{10}) gas at 100 mbar pressure that filled the ACTAR TPC
156 volume. At this pressure, the ^{18}O beam was stopped inside the active volume,
157 just above column number 98 (out of 128 total) of the pad plane. The maxi-
158 mum energy of the scattered protons was about 12 MeV, at 0° in the laboratory
159 frame. The corresponding energy deposited in the gas was $\frac{dE}{dx} = 1\,\text{keV/mm}$
160 ($2\,\text{keV/pad}$), which is the minimum energy deposit in the experiment. With
161 the MICROMEGAS mesh voltage set to -450 V, the gain was previously measured
162 to be 5000 in Ref. [16]. Hence, all proton tracks can be recorded with a trans-
163 verse multiplicity of three pads. This is necessary to achieve an optimal angle
164 reconstruction, and a good signal-to-noise ratio using the 120 fC GET preampli-
165 fier dynamic range, which corresponds to a gain of 180 mV/MeV Si equivalent.
166 However, the difference in energy deposit between ^{18}O ions stopping in the ac-
167 tive volume (about 100 keV/mm) and the recoiling protons was up to a factor
168 100.

169 As shown in Ref. [16], a single dynamic range of the GET preamplifiers is

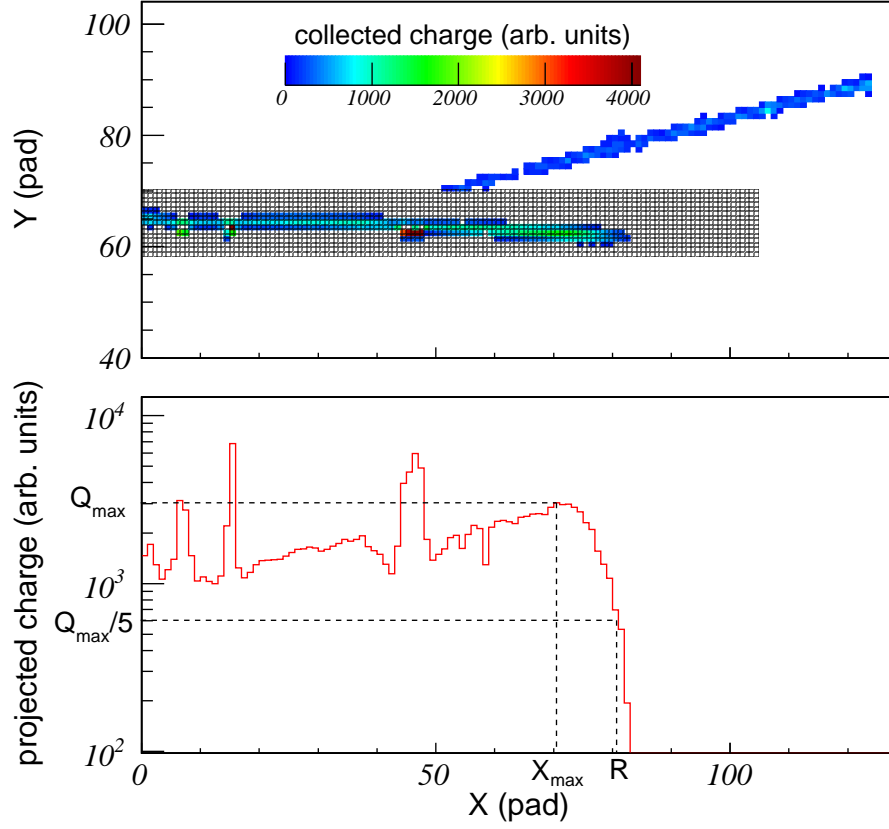


Figure 2: (color online) *Upper panel*, example of an event with the shaded polarization zone below the beam. *Lower panel*, projection of the beam particle along the X axis. The track stopping point R of the beam, plus the scattered heavy particle if there is a reaction as it is the case here, is defined as a fifth of the Bragg curve maximum charge deposit. The polarization could not be applied for some pads, due to connection problems, resulting in a significantly higher charge compared to their neighbours (around $X=10$ pad and $X=50$ pad), which results in the peaks shown in the reconstructed Bragg curve. These pads were discarded in the analysis.

not sufficient to record the track of the beam ions and the track of the protons at the same time without saturating the electronics. In order to extend the effective dynamic range, the pads located below the beam path were polarized to -100 V, locally reducing the gain of the MICROMEGAS from about 5000 to about 250. This follows the work described in Ref. [22].

With a beam emittance of about $\pi\sigma_x\sigma_\theta = 18.56\pi\text{ mm}\cdot\text{mrad}$, obtained by tracking the beam upstream from the reaction point, the width of the polarized zone was set to 12 rows of pads (24 mm) and was 100 columns (200 mm) in length, as shown in the upper panel of Figure 2. Due to connection problems, some of the pads from this zone could not be correctly polarized. As a result, the MICROMEGAS has a higher gain above those pads, which produces the peaks on the Bragg profile shown in the lower panel of Figure 2. The GET system was set to partial readout mode, so that only pads with a signal exceeding a certain threshold were read. This readout threshold was set to 5.3 fC, which corresponds to 3.27×10^4 electrons. With the MICROMEGAS gain of 5000, this threshold is about 6.6 ionization electrons, or about 0.2 keV energy deposited per pad.

The cathode voltage was set to -3500 V, so that the drift velocity of the ionization electrons was about $3.6\text{ cm}/\mu\text{s}$. The total time window required to observe the full height of the active volume was therefore $6.7\text{ }\mu\text{s}$. The sampling frequency of the GET system was set to 50 MHz, which provided a time window of $10.24\text{ }\mu\text{s}$ over 512 samples for detecting the ionization electrons. Following the definition of Ref. [23], the samples will be later referred to as *time cells*. The test experimental conditions are summarized in Table 1.

For later discussions on the analysis, we introduce the following terms:

- *Electronic events* are defined as the full window of 512 time cells over the whole pad plane.
- *Physical events* are defined as the grouping of tracks correlated in time/space.
- *Beam events* are defined as unreacted events, forming physical events only consisting of a beam track.

Table 1: Beam and detector settings used during the ACTAR TPC ^{18}O commissioning experiment.

Parameter	Value	Units
Beam energy at active volume entrance	57.6	MeV
Beam emittance	18.56π	mm·mrad
Average beam intensity	1.5×10^4	pps
Cathode potential	-3500	V
Mesh potential	-450	V
Polarized pads potential	-100	V
Drift velocity (measured)	3.8	cm/ μs
Isobutane gas pressure	100	mbar
Proton target density	2.5×10^{19}	protons/cm ³
Clock frequency	50	MHz
GET dynamic range	120	fC
GET readout threshold	5.3	fC
GET peaking time	1024	ns

- *Pileup events* are defined when there are several physical events in an electronic event.

3. Data analysis

3.1. Particle tracking

To extract the voxel information (the charge collected and the electron arrival time on each pad), the signal baseline was first treated using the methods described in Ref. [23]. After baseline treatment, the physical pulse was fit with a generic pulse shape as described in [24]. The timing information was translated into a vertical position using the electron drift velocity in the gas. By correlating the Si detector hit with the recoil nuclei tracked, the impact matrix on each Si detector can be reconstructed. The drift velocity is adjusted to match the reconstructed vertical size of the Si detector to 5 cm. The determined value of 3.8 cm/ μs is in agreement with the MAGBOLTZ [25] calculated velocity of 3.6 cm/ μs .

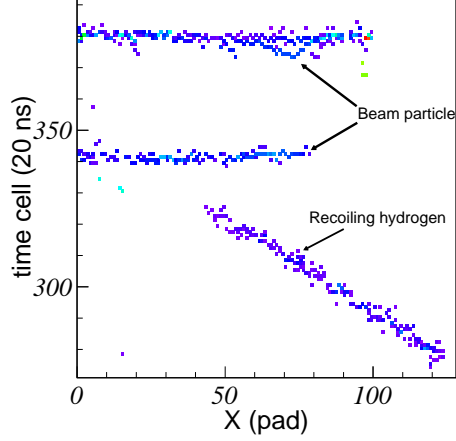


Figure 3: (color online) Example of pileup event observed in ACTAR TPC, two beam tracks are seen and only one recoil, corresponding to a reaction. The beam tracks that reacted has a shorter track. The beam track above corresponds to a beam event happening at a later time than the physical event below. The color scale indicates the charge deposit.

214 A typical event contains the beam track and the track of the heavy scattered
 215 ion that stops in the active volume. Given that the maximum scattering angle
 216 of the heavy ion does not exceed 15° for (p, α) reactions at the lowest measured
 217 reaction energy, the tracks directions are very close and are almost always con-
 218 fined to the polarized (low gain) region of the pad plane. For this reason, we
 219 consider in the analysis and define in the following that *beam tracks* are contin-
 220 uous tracks in the polarized beam region (Figure 2), meaning unreacted beam
 221 or the incoming beam plus the scattered heavy-ion, without distinction. Scat-
 222 tering events also contain the track of the light recoil particle that is observed
 223 in the unpolarized (high gain) zone. As seen in the upper panel of Figure 2,
 224 the pad plane can thus be separated into two areas: the polarized zone, that
 225 contains the tracks of the heavy ions, and the unpolarized zone that contains
 226 the tracks of the light recoils. Following this division, the tracking analysis is
 227 performed in each area independently. The track fitting procedure is adapted
 228 from the orthogonal distance regression presented in Ref. [26].

229 Due to the high beam intensity, the probability to record two incident beam
 230 particles in the same acquisition window of $10.24 \mu\text{s}$ is significant. A pileup

231 separation technique was therefore developed and applied to the polarized zone.
 232 Pileup events arrive at different times and are thus separated into different time
 233 cells, as shown in the example of Figure 3, which displays the charge projection
 234 of three particle tracks in the X-Z plane (X is the axis of propagation of the
 235 beam and Z the vertical axis along which the electrons drift). Comparing the
 236 recoiling particle timing (the track going down in Figure 3) and timing of the
 237 two separate beam tracks (horizontal tracks) in a single electronic event, the
 238 recoil and one beam track can be regrouped in a correlated physical event. In
 239 Figure 4, the amount of pileup per electronic event is plotted as a function of the
 240 beam intensity. For example, at a beam intensity of 10^4 particle per second (pps,
 241 left panel of Figure 4), only 12% of the electronic events recorded more than
 242 one beam track. When the beam intensity was doubled to 2×10^4 pps (right
 243 pane of Figure 4), 27% of the events were piled up. This is consistent with the
 244 expected Poisson time distribution of the beam. Using the pileup separation
 245 technique, close to 100% of these pileup events were recovered in the analysis.
 246 The separation limit is given by the time difference between two beam tracks
 247 compared to the beam track time width, due to the longitudinal straggling of
 248 the electrons as they drift toward the MICROMEGAS. In this commissioning, this
 249 width was consistent with the MAGBOLTZ calculation, that depends on the gas
 250 used and the magnitude of the drift electric field applied.

251 *3.2. Particle identification*

252 After tracking particles in the TPC, the second step of the analysis consisted
 253 in identifying the light recoil. This identification was performed by correlating
 254 the energy recorded in the silicon detectors E_{Si} with the energy loss in the gas
 255 per millimeter, averaged over the last 15 columns of pads. However, the mea-
 256 surement of the energy deposition in the gas is affected by attachment due to
 257 O₂ molecules. Indeed, during the experiment, a small air leak on the pad plane
 258 flange was detected. In order to estimate the proportion of air in the detector,
 259 several short runs were taken using the MWPC in front of ACTAR TPC as
 260 trigger, allowing the selection of unreacted beam events by looking at events

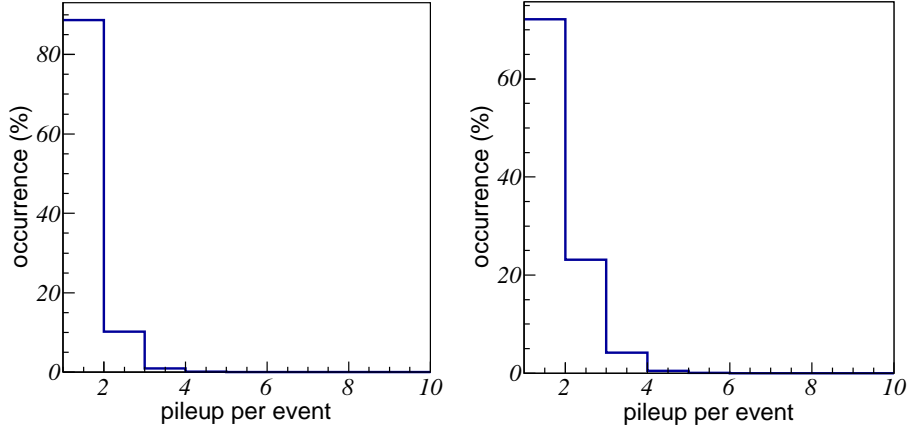


Figure 4: Occurrence of pileup events. A total of 12% of the events at 10^4 pps were piled up in ACTAR TPC (**left**). When the beam intensity was doubled this increased to 27% (**right**). Most of these events were recovered in the analysis by correlating the timing between the light recoil to one of the incident beam tracks (see text).

261 without energy deposit in the Si. The range of the beam particles was compared to LISE++ calculations [27] using the energy loss tables of Ref. [28]. A
 262
 263 2% air pollution was deduced and was found to be constant over the 20-hour
 264 experiment. Drift electron attachment to the O_2 molecules caused the charge
 265 recorded over the pad plane to depend exponentially on the position (height
 266 above the anode) in which the ionization electrons were produced. The information
 267 on the energy deposited had to be corrected for this effect by applying a
 268 factor that varied exponentially with the drift distance. With the silicon trigger,
 269 the number of time cell can be directly transformed into a drift distance for the
 270 triggering event. Then, the exponential correction parameters were determined
 271 from the correlation between the energy loss measured over the pad plane of
 272 25 MeV α particles recorded in the silicon detectors, and the known mean drift
 273 distance of their tracks. α particles are identified by the fact that the proton
 274 punch-through is at 10 MeV and only negligible amount of other particles are
 275 expected to reach the silicon detectors. The correlation is shown in the inset of
 276 Figure 5, with the exponential fit (correction factor) drawn through the data
 277 points. The attachment parameter extracted from a fit of this 2D plot reaches

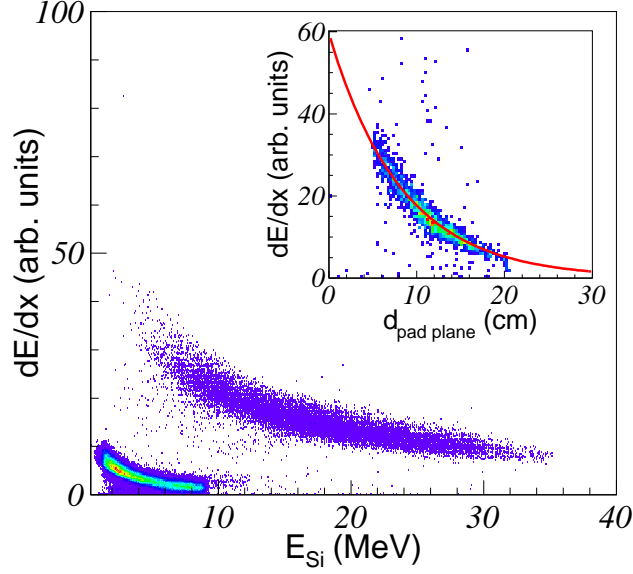


Figure 5: (color online) Particle identification using the energy deposit over the pad plane versus the energy lost in the silicon detectors after correction of the height dependence. The energy deposit is averaged over the last 15 columns of pads. The identification lines observed correspond to hydrogen and helium. In the inset, the correlation of the energy deposit over the pad plane with respect to the distance between the pad plane and the hit position on the Si detector extracted from the track fit is plotted for $E_{\text{Si}} = 25 \pm 1$ MeV. The solid red line corresponds to the applied correction function.

278 $\lambda_a = 0.126 \text{ cm}^{-1}$, about a factor 10 above the value deduced with MAGBOLTZ.
 279 After applying this correction, the identification plot presented in Figure 5 was
 280 obtained. Without the correction factor, the identification lines width in $\frac{dE}{dx}$
 281 would spread about four times more.

282 3.3. Reaction channel selection

283 In the present experiment, four reaction channels are open. Two of them
 284 have a proton and an ^{18}O in the final state: the elastic channel and the inelas-
 285 tic channel to the first excited state of ^{18}O in the highest energy part of the
 286 excitation function. Two other reactions have an α in the final state together
 287 with a ^{15}N either in its ground state or in its first excited state. If the parti-
 288 cle identification can be achieved with the classic thick solid target in inverse

289 kinematics method [29, 30], active targets offer a unique possibility to select the
 290 excitation energy in the final state. This is achieved through the tracking of
 291 the heavy particle, or more precisely, by the determination of the total path of
 292 the beam plus scattered heavy particle after reaction in the active volume R .
 293 This can be extracted by projecting the charge collected on the pad plane po-
 294 larized area along the X-axis (Figure 2). The beam energy-loss profile along the
 295 X-axis is constructed and the beam-like particle stopping point is determined.
 296 As defined in the lower panel of Figure 2, it corresponds to the point where the
 297 charge value has decreased to a fifth of the Bragg peak maximum charge, which
 298 corresponded best to the SRIM energy loss tables [31].

299 As explained in [32, 33], if the center-of-mass angle of the reaction is fixed,
 300 there is a unique relationship between E_{Si} and R to the reaction energy and the
 301 excitation energy in the final state. Correlation plots for ${}^1\text{H}({}^{18}\text{O}, {}^{18}\text{O}){}^1\text{H}$ and
 302 ${}^1\text{H}({}^{18}\text{O}, {}^{15}\text{N}){}^4\text{He}$ are presented in Figure 6 for $160 \pm 5^\circ$ center-of-mass, selected
 303 with the proton or α -particle laboratory angle. This angle was chosen for com-
 304 parison with the measurements of Ref. [34]. The zero of the abscissa corresponds
 305 to the start of the pad plane. The events corresponding to the population of
 306 the ground state of ${}^{18}\text{O}$ and ${}^{15}\text{N}$ can be identified on the figure. Though ener-
 307 getically allowed, no events corresponding to the population of the first excited
 308 state of ${}^{18}\text{O}$ and ${}^{15}\text{N}$ were observed. This is consistent with the measurement
 309 of Ref. [34]. The vertical lines observed in Figure 6 come from pileup events
 310 when $R \simeq 20$ cm. Below 20 cm, they come from the information lost due to the
 311 unpolarized pads described previously and shown in Figure 2. On the right of
 312 Figure 6, points can also be observed below the ${}^{15}\text{N}$ ground state line. Most of
 313 these correspond to fusion reactions with ${}^{12}\text{C}$ in the iC_4H_{10} gas and evapora-
 314 tion of an α -particle. They can be partially identified because the Bragg peak
 315 maximum of ${}^{26}\text{Mg}$ is about 80% larger than ${}^{15}\text{N}$. This identification can be ten-
 316 tatively performed for reactions before pad 50. Beyond that point, the reaction
 317 energies are below 20 MeV. At the center-of-mass angles used in the analysis,
 318 this corresponds to ${}^{26}\text{Mg}$ with an energy below 2.5 MeV, beyond the Bragg peak.
 319 The energy deposited by ${}^{26}\text{Mg}$ is then indistinguishable from ${}^{15}\text{N}$. In this case,

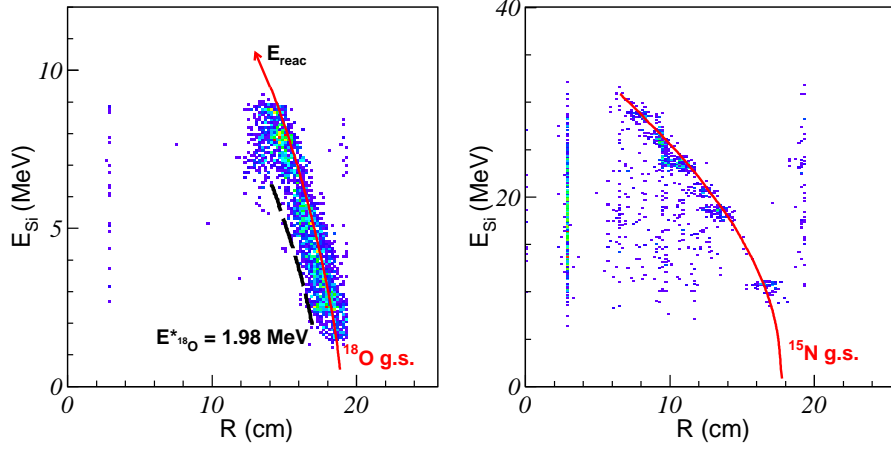


Figure 6: (color online) Identification of the kinematic line corresponding to the ground state of the beam like particle, at $\theta_{\text{cm}} = 160 \pm 5^\circ$. The total energy left in the Si detector E_{Si} is plotted as a function of the total path R (Figure 2).

identification of the heavy particle before pad 50 is not performed because of the unpolarized pads in the beam area (Figure 2). As fusion-evaporation is not kinematically allowed above the $^1\text{H}(^{18}\text{O}, ^{15}\text{N})^4\text{He}$ ground state kinematic line, these reactions provide a source of background that can be largely suppressed by selecting the ^{15}N ground-state line.

3.4. Construction of the excitation function

After selecting the reaction channel, the reaction energy was reconstructed using an iterative procedure. The reaction kinematics was used to calculate the reaction energies. Having the energy deposited in the Si detectors E_{Si} and the track angle θ_{lab} fitted from the TPC voxels, the reaction energy E_{reac} was determined using the formula:

$$E_{\text{reac},i} = \frac{m_{^{18}\text{O}}(m_{\text{H}}/m_{^{18}\text{O}} + 1)^2 E_{\text{H},i}}{4m_{\text{H}} \cos^2(\theta_{\text{lab}})} \quad (1)$$

for the case of the (p,p) channel, with i the iteration number. m_{H} and $m_{^{18}\text{O}}$ are the proton and ^{18}O atomic masses, respectively. E_{H} is the total energy of the recoiling proton. At the first iteration, $E_{\text{H},0} = E_{\text{Si}}$. With the calculated $E_{\text{reac},0}$,

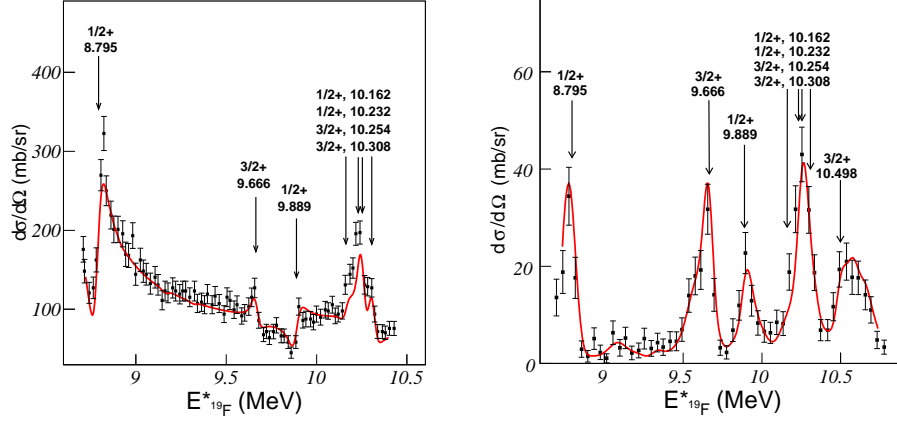


Figure 7: Excitation energy of ^{19}F from the (p,p) channel on the left and from the (p, α) channel on the right projected for $\theta_{\text{cm}} = (160 \pm 5)^\circ$. The black dots with statistical uncertainties are the experimental points and the red curve is the result of the R-matrix calculation convoluted with a Gaussian function that was fit the data (see text for details). Resolutions were found to be 38(4) keV FWHM and 54(9) keV FWHM, respectively.

and assuming the known initial beam energy E_{beam} , the vertex position was calculated using energy-loss tables [31]. From the measured vertex position, it is possible to determine the energy lost by the light particle in the gas, dE_0 , before it arrives at the silicon detector. $E_{\text{reac},1}$ is calculated using $E_{\text{H},1} = E_{\text{Si}} + dE_0$ and θ_{lab} , leading to another vertex position. The recoil energy is corrected again : $E_{\text{H},i+1} = E_{\text{Si}} + dE_i$. This procedure is repeated until $|dE_i - dE_{i-1}| < 1 \text{ keV}$. The entire procedure takes between 2 and 4 iterations. The same procedure was performed for the (p, α) channel with the corresponding kinematic formula. The excitation functions at $\theta_{\text{cm}} = (160 \pm 5)^\circ$ for both (p,p) and (p, α) channels are presented in Figure 7. The absolute normalization of the data used the MWPC counter after correcting the data by the detection efficiency of the ACTAR TPC. The latter was determined using a Monte Carlo simulation that includes the geometry of the pad plane and the position of the silicon detectors. At $\theta_{\text{cm}} = 160^\circ$, the efficiency was found to vary between 90 % and 100 % depending on the center-of-mass energy.

349 4. Results and Discussion

350 In order to estimate the resolution of ACTAR TPC on the center-of-mass
 351 energy reconstruction, the data were fit with a theoretical model convoluted
 352 with a Gaussian function to represent the experimental energy resolution. In
 353 the case of the (p,p) channel, the theoretical model is an R-matrix calculation
 354 performed with the AZURE2 code [35]. All resonance energies and widths that
 355 are available on ENSDF [36] were considered in the calculation. For the case of
 356 the (p, α) channel, the lack of data on ENSDF led us to use a different approach.
 357 The data obtained in a previous study [34] were used as the theoretical model.
 358 The uncertainty on the center-of-mass energy in Ref. [34] are much smaller than
 359 in our experiment, hence the model was considered as having perfect resolution.
 360 The result of the fits are presented in Figure 7. The resonances available on
 361 ENSDF or Ref. [34] are indicated by the arrows on the plot. Resolution on
 362 the center-of-mass energy for the (p,p) and (p, α) channels were found to be
 363 38(4) keV FWHM and 54(9) keV FWHM, respectively.

364 In order to better understand where this resolution was coming from, the
 365 uncertainties on the different experimental parameters were propagated to the
 366 center-of-mass energy determination by a Monte-Carlo calculation. From sec-
 367 tion 3.4, the parameters used to reconstruct the excitation function are:

- 368 • the beam energy at the entrance of ACTAR TPC E_{beam} ;
- 369 • the energy deposited by the light recoil in the silicon detectors E_{Si} ;
- 370 • the light recoil diffusion angle θ_{lab} .

371 The resolution on E_{beam} primarily comes from the energy straggling produced
 372 by the 63 μm thick aluminum degrader and the 6 μm Mylar entrance window.
 373 This was estimated using unreacted beam events triggered by the MWPC as
 374 explained previously. The distribution of the beam reconstructed stopping point
 375 position had a lateral spread of $\sigma = 6$ mm that was translated using SRIM tables
 376 into an energy spread of 1.5 MeV FWHM. The resolution on E_{Si} was determined
 377 using a $^{239}\text{Pu} + ^{241}\text{Am} + ^{244}\text{Cm}$ mixed alpha-particle source. It was assumed

Table 2: Propagation of the parameter resolution to the excitation function. All values are given in FWHM. θ_{lab} has the largest contribution to the resolution. Details on the parameter resolutions are given in the text.

Parameter	Resolution	Propagation to E_{cm} (keV)	
		(p,p) channel	(p, α) channel
E_{beam}	1.5 MeV	8.5	17.4
E_{Si}	60 keV	16.5	21.1
θ_{lab}	2°	22.3	34.8
Total simulation		29	45
Experimental		38(4)	54(9)

378 to vary linearly with the energy. The resolution on E_{Si} was found to be 60 keV
 379 FWHM at 5.5 MeV. The resolution on θ_{lab} was measured using the shape re-
 380 construction of the central Si detectors. This was achieved by tracking particles
 381 that hit the central silicon detector, and extrapolating the track to the plane of
 382 the silicon detector. The θ_{lab} resolution had a maximum value of 2° FWHM.
 383 The measured resolution was estimated to be mostly due to the straggling of the
 384 recoils in the gas. For comparison, protons recorded with an energy of 3 MeV in
 385 the Si detectors travelled at least through 175 mm of gas based on the reaction
 386 kinematics. When calculated with LISE++, the associated angular straggling is
 387 1.8° FWHM for the proton. This is in reasonable agreement with the measured
 388 angular resolution. From the LISE++ calculations, the recoiling α should have
 389 a better angular resolution of 0.84° FWHM for a 25 MeV recorded α traveling
 390 284 mm of gas. The statistics on α particles was too small to measure the an-
 391 gular resolution in the same way. Since this factor has the greatest influence on
 392 the center-of-mass resolution, it was taken as 2° for the (p, α) channel as well so
 393 as to not underestimate its effect. A summary of the parameter resolutions and
 394 the propagation on the final simulated resolutions are given in Table 2. The
 395 propagated uncertainties are consistent with the experimental result.

5. Conclusion

We have characterized the performance of a novel active target and detection system that does not rely on a magnetic spectrometer. The next generation active target ACTAR TPC was commissioned at the GANIL facility with a 3.2 MeV/nucleon ^{18}O beam with an average beam intensity of 1.5×10^4 pps on isobutane gas. The challenge of the energy loss discrepancy by a factor 100 between the stopping heavy-ions and the light recoils was met with the polarization of the pads below the beam. It was successful in producing two gain regions with an incident beam intensity of 20 kHz without degrading the charge measurement. The $^1\text{H}(^{18}\text{O}, ^{18}\text{O})^1\text{H}$ and $^1\text{H}(^{18}\text{O}, ^{15}\text{N})^4\text{He}$ channels were open and could be distinguished with the scattered heavy-ion identified as being in its ground state. The excitation functions in both channels were reconstructed and fit to obtain the center-of-mass energy resolutions. Resolutions of 38(4) keV FWHM for the (p,p) channel and 54(9) keV FWHM for the (p, α) channel were achieved. According to simulations, the resolution is dominated by the angular resolution, which itself is dominated by the straggling of the ions in the gas. The latter could be decreased by replacing the isobutane gas target by pure hydrogen. The present resolution is comparable to the 45 keV center-of-mass energy resolution achieved with the Active-Target Time Projection Chamber (AT-TPC) from Michigan State University that was measured for the $^1\text{H}(^{46}\text{Ar}, ^{46}\text{Ar})^1\text{H}$ reaction [13, 37]. This resolution was obtained with a factor 10 less beam intensity for center-of-mass angles between 30° and 65° , and with a direct measurement of the reaction point in the active target. Using the reaction kinematics, as performed in the present work, the AT-TPC has an expected resolution of 84 keV derived from simulations of the $^1\text{H}(^{46}\text{Ar}, ^{46}\text{Ar})^1\text{H}$ [13]. Unfortunately, no experimental measurement was made with the AT-TPC to confirm this result due to challenges associated with the experimental data obtained in Ref. [13].

The new technological developments for active targets have opened up new possibilities to perform challenging reactions for nuclear structure and astrophysical studies. The results of the present study show that ACTAR TPC

426 holds considerable promise in this respect.

427 **Acknowledgments**

428 The research leading to these results have received funding from the Euro-
429 pean Research Council under the European Union’s Seventh Framework Pro-
430 gram (FP7/2007-2013)/ERC grant agreements n° 335593 and 617156, and from
431 the Research Foundation Flanders (FWO, Belgium).

432 **References**

- 433 [1] S.Beceiro-Novo *et al.*, Prog. in Part. and Nucl. Phys. **84** (2015) 124
- 434 [2] G. D. Alkhazov *et al.*, Phys. Rev. Lett. **78** (1997) 2313
- 435 [3] C.-E. Demonchy *et al.*, Nucl. Instr. and Meth. A **583** (2007) 341
- 436 [4] M. Caamaño *et al.*, Phys. Rev. Lett. **99** (2007) 062502
- 437 [5] I. Tanihata *et al.*, Phys. Rev. Lett. **100** (2009) 192502
- 438 [6] T. Roger *et al.*, Phys. Rev. C **79** (2009) 031603(R)
- 439 [7] C. Monrozeau *et al.*, Phys. Rev. Lett. **100** (2008) 042501
- 440 [8] M. Vandebrouck *et al.*, Phys. Rev. Lett. **113** (2014) 032504
- 441 [9] B. Blank *et al.*, Nucl. Instr. and Meth. A **613** (2010) 65
- 442 [10] P. Ascher *et al.*, Phys. Rev. Lett. **107** (2011) 102502
- 443 [11] E.C. Pollacco *et al.*, Nucl. Instr. and Meth. A **887** (2018) 81-93
- 444 [12] S. Ota *et al.*, J. Radioanal. Nucl. Chem. 305 (2015) 907911
- 445 [13] J. Bradt *et al.*, Nucl. Instr. and Meth. A 875 (2017) 6579
- 446 [14] T. Furuno *et al.*, Nucl. Instr. and Meth. A 908 (2018) 215224
- 447 [15] J. Hooker *et al.*, arXiv:1903.01402

- 448 [16] T. Roger *et al.*, Nucl. Instr. and Meth. A **895** (2018) 126-134
- 449 [17] J. Giovinazzo *et al.*, Nucl. Instr. and Meth. A **892**, (2018) 114
- 450 [18] I. Giomataris *et al.*, Nucl. Instr. and Meth. A **376**, (1996) 29
- 451 [19] I. Giomataris *et al.*, Nucl. Instr. and Meth. A **560**, (2006) 405
- 452 [20] J. Pancin *et al.*, Nucl. Instr. and Meth. A **735**, (2014) 532
- 453 [21] G. Wittwer , Clock Event Number Transmitter Receiver Universal Module,
454 Users Manual , GANIL July 2004
- 455 [22] D. Suzuki *et al.*, Nucl. Instr. and Meth. A **660**, (2011) 64-68
- 456 [23] J. Giovinazzo *et al.*, Nucl. Instr. and Meth. A **840** (2016) 15-27
- 457 [24] G. Jhan, *Workshop on Active Targets and Time Projection Chambers for*
458 *High-intensity and Heavy-ion beams in Nuclear Physics* (2018)
- 459 [25] magboltz.web.cern.ch/magboltz/
- 460 [26] T. Roger *et al.*, Nucl. Instr. and Meth. A **638**, (2011) 134-142
- 461 [27] O.B. Tarasov, D.Bazin, Nuclear Physics A **746**, (2004) 411c-414c
- 462 [28] J.F. Ziegler, J.P. Biersack, U. Littmark, *The stopping and range of Ions in*
463 *Solids*, Pergamon, New York, 1985
- 464 [29] K. Artemov *et al.*, Sov. J. Nucl. Phys. **52**, 408 (1990)
- 465 [30] V. Z. Goldberg and A. E. Pakhomov, Phys. At. Nucl. **56**, 1167 (1993)
- 466 [31] J. Ziegler , <http://www.srim.org/>
- 467 [32] C.-E. Demonchy, PhD. Thesis, Université de Caen (2002) [https://tel.](https://tel.archives-ouvertes.fr/tel-00004117)
468 [archives-ouvertes.fr/tel-00004117](https://tel.archives-ouvertes.fr/tel-00004117)
- 469 [33] T. Roger, PhD. Thesis, Université de Caen (2009) [https://tel.](https://tel.archives-ouvertes.fr/tel-00424010)
470 [archives-ouvertes.fr/tel-00424010](https://tel.archives-ouvertes.fr/tel-00424010)

- 471 [34] R.R. Carlson *et al.*, Physical Review **122**, 607-616 (1961)
- 472 [35] R. Azuma *et al.*, Phys. Rev. C **81**, 045805, (2010)
- 473 [36] ENSDF, <http://www.nndc.bnl.gov/ensdf/>
- 474 [37] J. Bradt *et al.*, Phys. Lett. B **778**, 155, (2018)

Dear Editor,

Referee 1 asked us to expand the abstract and update the conclusion to give a better explanation and summary of the work performed in the present article. In this updated submission we have now done so, taking into account all of the Referee's suggestions. All other minor changes suggested by the referee (roman font on cm, definition of iC_4H_{10} , wording updates on other lines) have also been fully included in the present version. We again wish to thank the Referees for their detailed report and careful reading of our manuscript.